Nano Research

Open Access

Research Article

Multicore–shell bismuth nanoparticles@N-doped porous carbon nanorods for dendrite-free zinc metal anodes

Yushuang Zheng[1,§], Yang Li[2,§], Xuan Zhang[3], Jie Xu[1], Bo Peng[1], Guoyin Zhu[3]✉, Jiapeng Liu[4]✉, and Lianbo Ma[1]✉

[1] School of Materials Science and Engineering, Anhui University of Technology, Maanshan 243002, China
[2] Department of Mechanical and Aerospace Engineering, The Hong Kong University of Science and Technology, Hong Kong, China
[3] Institute of Advanced Materials and Flexible Electronics (IAMFE), School of Chemistry and Materials Science, Nanjing University of Information Science and Technology (NUIST), Nanjing 210044, China
[4] School of Advanced Energy, Sun Yat-Sen University, Shenzhen 518107, China
§ Yushuang Zheng and Yang Li contributed equally to this work.

Cite this article: *Nano Research*, **2025**, *18*, 94907372. https://doi.org/10.26599/NR.2025.94907372

ABSTRACT: Aqueous zinc (Zn)-based batteries with high cyclic stability, exceptional safety, and low cost hold great promise as next-generation energy storage devices. However, Zn metal anode suffers from serious dendrite growth, hydrogen evolution, and Zn corrosion during plating/stripping cycles, hampering its practical utilization. Herein, we report a multicore–shell structure of bismuth (Bi) nanoparticles embedded within N-doped porous carbon nanorods (NPCN) (Bi@NPCN) to regulate Zn deposition behavior. Theoretical simulation and *in situ* optical microscopy revealed that the abundant Bi nanoparticles with high zincophilic property strongly adsorbed Zn^{2+}, enabling rapid and massive Zn deposition. Meanwhile, NPCN with porous feature provides sufficient space for accommodating Zn volume expansion. Electrochemical tests demonstrated an ultra-stable dendrite-free Zn deposition behavior for 1500 h, high rate capability up to 20 $mA \cdot cm^{-2}$, and an exceptional Coulombic efficiency of ~ 100% after 1200 cycles. The Zn-ion batteries coupled with ammonium vanadate cathode exhibit a highly-stable cyclic performance for 3000 cycles at 5.0 $A \cdot g^{-1}$, with a high capacity retention of 66.7%. Impressively, a remarkable long-term cyclic performance over 10,000 cycles was realized when employing active carbon cathode. This study offers a new strategy of utilizing multicore–shell structure with zincophilic seeds to achieve dendrite-free Zn metal anode.

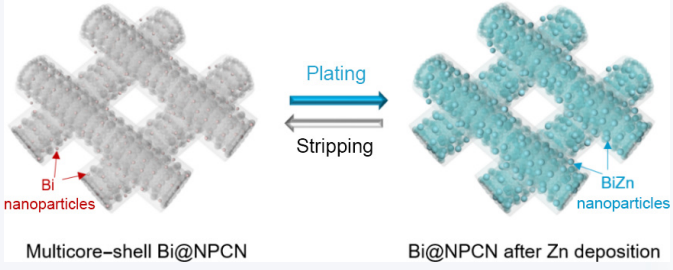

KEYWORDS: zinc metal anode, dendrite, multicore–shell, Bi nanoparticle, porous carbon nanorod

1 Introduction

The rapid development of modern electronic markets requires advanced energy storage devices with high stability and great safety [1, 2]. However, the traditional battery systems usually involve the utilization of highly-active metal anodes and carbonate/ether-based electrolytes [3, 4], which would inevitably induce safety issue. Recently, aqueous zinc (Zn)-based batteries, like Zn-ion batteries [5, 6] and Zn-iodine batteries [7, 8], have caught tremendous interests, owing to the high theoretical capacity, exceptional long-term cyclic stability, extremely-high safety, and nontoxicity [9, 10]. More importantly, Zn element reserves are abundant in earth's crust, significantly lowering the battery costs [11]. Nevertheless, Zn metal anode would suffer from uneven Zn deposition and dendrite formation/growth, leading to the generation of "dead Zn" and even short circuit of batteries [12–14]. Additionally, hydrogen evolution and Zn corrosion in aqueous electrolyte may occur during cycles, thereby further deteriorating the electrochemical performance of Zn metal anode [15–17].

To address the challenges facing Zn metal anodes, promising solutions have been attempted. Initially, similar to those in lithium/sodium metal anodes [18, 19], Zn host materials and new Zn structures with large surface areas were elaborately constructed to reduce the local current density and accommodate the volume

Received: February 10, 2025; **Revised:** March 11, 2025
Accepted: March 14, 2025

✉Address correspondence to Guoyin Zhu, gyzhu@nuist.edu.cn; Jiapeng Liu, liujp59@mail.sysu.edu.cn; Lianbo Ma, mlb8976@ahut.edu.cn

expansion of Zn anode [20, 21], but these strategies failed when significantly increasing Zn deposition currents. For instance, carbonaceous materials with micro- and nanostructures were employed as Zn host [22, 23], and the generation of Zn dendrite on surface can be put off efficiently but cannot be prevented. Another huge challenge should be the inhomogeneous electric field nearby Zn surface [24, 25], resulting in uneven Zn deposition and further dendrite growth. As a representative solution, protective layers were utilized to stabilize Zn metal anode [26, 27]. However, these kinds of strategies still cannot realize the uniform distribution of Zn^{2+} during persistent plating.

Recently, it is recognized that adopting zincophilic seeding sites can significantly address the issues facing Zn metal anode. The zincophilic seeding sites usually possess high chemical affinity with Zn^{2+} and low energy barriers for Zn nucleation and further deposition, improving Zn utilization ratio and meanwhile alleviating Zn dendrite formation and growth [28]. By far, several zincophilic seeds, like cobalt [29], silver [30], gold [31], copper [32], Sn [33, 34], and Zn [35], have been developed. However, these zincophilic seeds loaded on Zn surface or other substrates normally possess low loading amounts. Zn deposition initially occurs on the surface of Zn or substrates, but the continuous Zn deposition would inevitably induce the generation of Zn dendrites. Similarly, these zincophilic seeds within substrates usually exhibit limited active site number, restricting Zn deposition speed and leading to Zn dendrite formation/growth during long-time plating/stripping cycles. Therefore, it is urgently necessary to design and construct an intriguing structure with abundant zincophilic seeding sites.

Herein, we report a multicore–shell structure comprising of bismuth (Bi) nanoparticles encapsulated within N-doped porous carbon nanorods (NPCN) (Bi@NPCN) as a coating layer on separator to regulate Zn deposition behaviors. Notably, the utilization of Bi@NPCN coating layer realizes the synergistic effects of both Zn host and separator modification strategies. The Bi nanoparticles serve as zincophilic seeding sites, strongly adsorbing Zn^{2+} and effectively lowering the energy barriers for Zn nucleation and further deposition. NPCN in Bi@NPCN provides a uniform electric field, enabling homogeneous Zn^{2+} distributions during plating. More importantly, the multicore–shell structure of Bi@NPCN with sufficient space can afford much amount of Zn, facilitating the stability and longevity of Zn metal anode. The *in situ* optical microscopy reveals a completely dendrite-free Zn deposition under a high current rate for a long time. Electrochemical tests disclosed a stable cyclic performance for over 1500 h, high rate capability up to 20 $mA \cdot cm^{-2}$, and an exceptional Coulombic efficiency of ~ 100% for 1200 cycles. Impressively, when coupled with ammonium vanadate ($NH_4V_4O_{10}$) cathode, Zn-ion batteries exhibit a long-term cycle for 3000 times with a high capacity retention of 66.7%. Moreover, Zn-ion batteries using active carbon cathode display an ultra-stable cyclic performance for over 10,000 cycles at 5.0 $A \cdot g^{-1}$.

2 Results and discussion

The multicore–shell Bi@NPCN was fabricated through a typical two-step route (Fig. 1(a)). Bi-based metal–organic framework (Bi-MOF) was first synthesized via a hydrothermal method. Subsequently, during the temperature ramping process, the organic species converted into carbon matrix, and Bi species aggregated together and formed Bi nanoparticles. After further pyrolyzing with the assistance of diammonium dicyanide, partial Bi was evaporated, and space was generated between residual Bi and carbon shell,

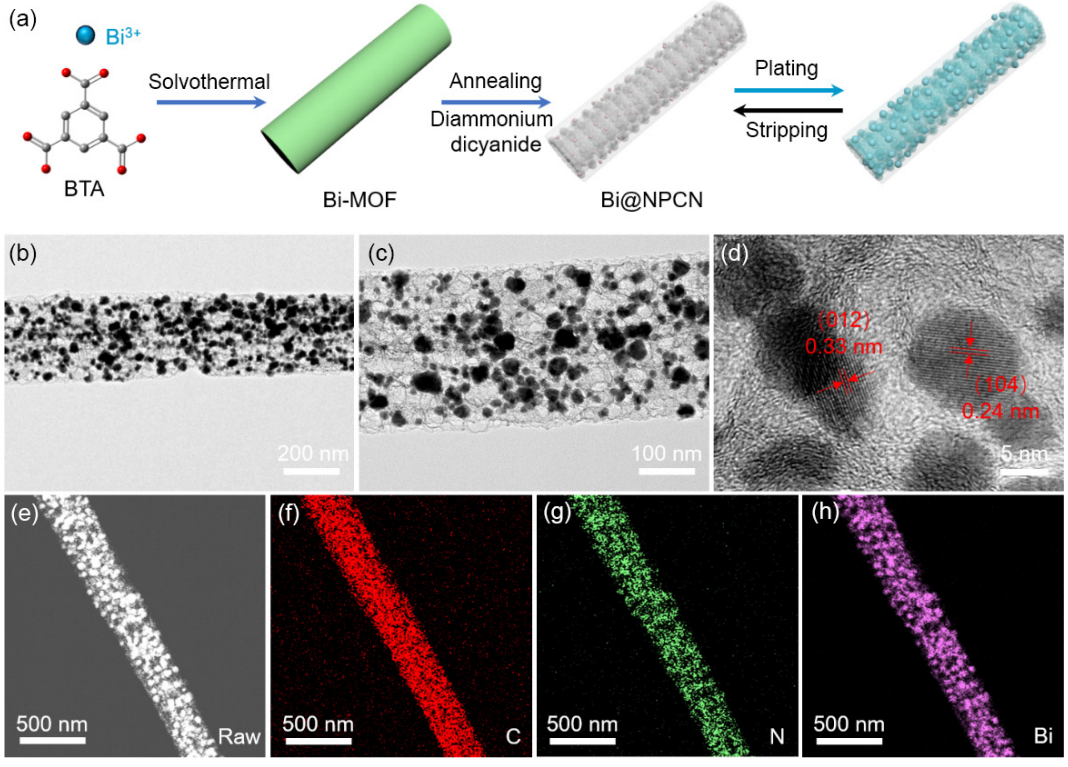

Figure 1 Synthesis and typical morphology of the as-prepared Bi@NPCN. (a) Schematic illustration of the synthesis of Bi@NPCN and its function during Zn plating/stripping cycles. BTA: 1,3,5-benzenetricarboxylic acid. (b) and (c) TEM, (d) HRTEM, and (e) HAADF-STEM images and (f)–(h) elemental mapping results of Bi@NPCN.

creating multicore–shell Bi@NPCN. Particularly, diammonium dicyanide under high temperature can release ammonia, simultaneously serving as the reduction agent and N-doping source. Figure S1 in the Electronic Supplementary Material (ESM) shows the transmission electron microscopy (TEM) images of Bi-MOF, revealing a nanorod morphology. TEM image with higher magnification indicates the smooth surface of Bi-MOF, and discloses an average width of ~ 300 nm. After the pyrolysis process, the product inherits the nanorod morphology of Bi-MOF, as displayed in Fig. 1(b), and numerous nanoparticles are observed. Further TEM image (Fig. 1(c)) demonstrates the uneven and coarse surface characteristic with porous inner structure of Bi@NPCN. Notably, small nanoparticles are completely embedded within the pores (Fig. 1(d)), forming a multicore–shell structure. The high-resolution TEM (HRTEM) image indicates that the average particle size of Bi is ~ 10 nm and further reveals two lattice distances of 0.33 and 0.24 nm, corresponding to the (012) and (104) planes of Bi, respectively. Figures 1(e)–1(h) show the high-angle annular dark-field scanning transmission electron microscopy (HAADF-STEM) image and corresponding elemental mapping results. Obviously, C, N, and Bi elements are achieved, and their homogeneous distributions within multicore–shell Bi@NPCN are further demonstrated. As a control sample, NPCN shows the similar morphology and structure, but without the existence of Bi nanoparticles (Fig. S2 in the ESM). The HAADF-STEM results disclose the existence and uniform distributions of C and N elements within NPCN.

The compositions and crystalline structure of the as-prepared samples were further investigated. As displayed in Fig. 2(a), the XRD patterns of Bi@NPCN and NPCN disclose the representative diffraction peaks of carbonaceous materials. Particularly, the diffraction peaks belonging to Bi metal were also observed from Bi@NPCN (JCPDS card No. 44-1246). Figure 2(b) presents the Raman spectra of both Bi@NPCN and NPCN, showing the typical Raman D and G bands originating from carbon materials. This is consistent with the XRD results. The intensity ratio of D to G bands (I_D/I_G) for Bi@NPCN and NPCN are calculated to be 1.05 and 0.98, respectively, suggesting the moderate graphitic degree of carbon matrices [36, 37]. Notably, the slightly higher I_D/I_G value for Bi@NPCN may be attributed to the short annealing time compared to that of NPCN and the defects induced by Bi nanoparticles. Figure 2(c) shows the nitrogen adsorption and desorption isotherms of Bi@NPCN and NPCN, disclosing the typical micro- and mesoporous feature of NPCN. The Brunauer–Emmett–Teller (BET) surface areas of both Bi@NPCN and NPCN are about 25.4 and 286.0 $m^2 \cdot g^{-1}$, respectively, and their corresponding Barrett–Joyner–Halenda (BJH) pore volumes are 0.13 and 1.03 $cm^3 \cdot g^{-1}$, respectively (Fig. 2(d)). The X-ray photoelectron spectroscopy (XPS) was conducted to further probe the chemical states and valences of the compositions. As shown in Fig. S3 in the ESM, the survey XPS spectrum of Bi@NPCN indicates the presence of C, N, and Bi elements, but no Bi element was detected from that of NPCN (Fig. S4(a) in the ESM). The high-resolution XPS spectrum at N 1s region for Bi@NPCN reveals three N groups (Fig. 2(e)), including pyridine-N at 398.2 eV, pyrrole-N at 399.8 eV, and graphitic-N at 401.6 eV [38]. The high-resolution XPS spectrum at N 1s region for NPCN discloses three similar N groups (Fig. S4(b) in the ESM). The high-resolution XPS spectrum at Bi 4f region shows two strong peaks located at 158.8 and 164.2 eV (Fig. 2(f)), ascribing to the Bi $4f_{7/2}$ and Bi $4f_{5/2}$, respectively. This indicates that the valence state of Bi in Bi@NPCN is positive, which can be attributed to the unavoidable partial surface oxidation of Bi. Notably, although oxidized Bi surface was detected, the bulk was still Bi metal, and only rhombohedral phase Bi was analyzed by XRD and TEM characterizations [39, 40].

To evaluate the crucial roles of the as-prepared samples for guiding Zn deposition behaviors, symmetrical batteries were firstly assembled by using Zn foil as both working and counter electrodes, bifacially modified glass fiber (GF) membrane as separator, and 2.0 M $ZnSO_4$ as the electrolyte. Symmetrical batteries using pristine GF membrane were also tested for comparison. Figure S5 in the ESM presents the electrochemical impedance spectroscopy (EIS) spectra of these symmetrical batteries, which are composed of a semicircle. Notably, the symmetrical batteries using Bi@NPCN-

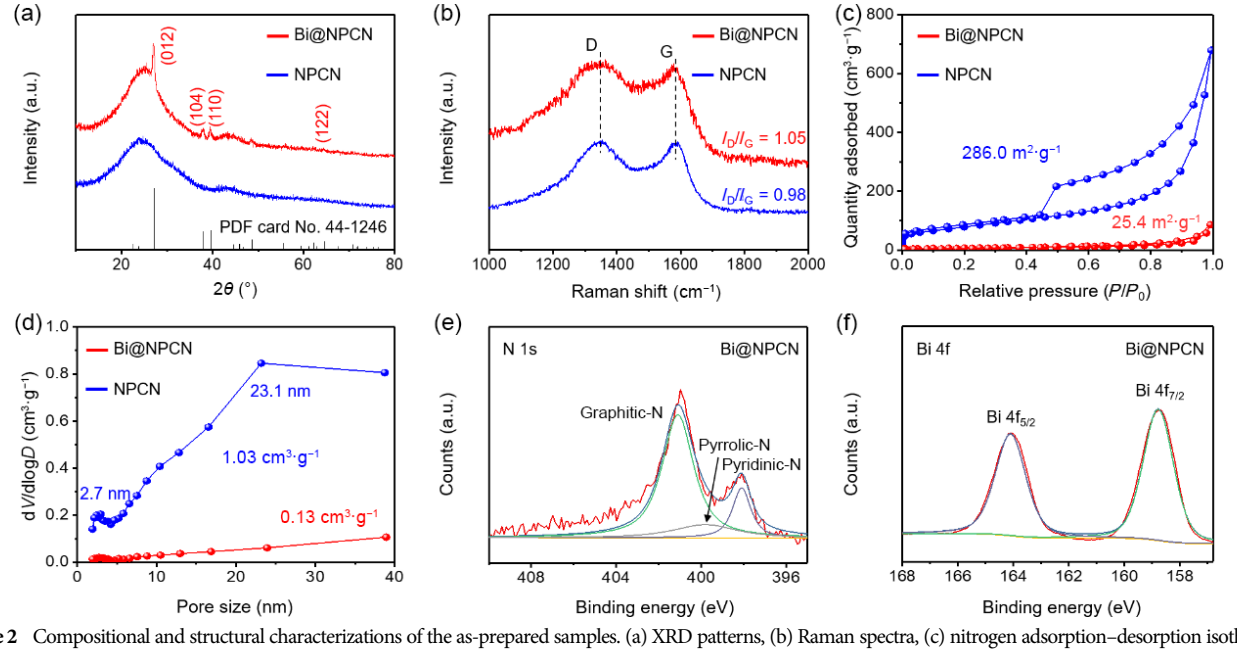

Figure 2 Compositional and structural characterizations of the as-prepared samples. (a) XRD patterns, (b) Raman spectra, (c) nitrogen adsorption–desorption isotherms, and (d) pore size distribution curves of Bi@NPCN and NPCN. High-resolution XPS spectra at (e) N 1s and (f) Bi 4f regions.

modified separator shows the smallest diameter, indicating the lowest charge transfer resistance. The cyclic stability of Zn plating/stripping behaviors for these symmetrical batteries was then investigated. As displayed in Fig. 3(a), the symmetrical batteries using Bi@NPCN-modified separator show an outstanding reversibility for over 1500 h under 1 mA·cm^{-2} and 1 mAh·cm^{-2}. As sharp contrasts, the symmetrical batteries using NPCN-modified separator and pristine GF membrane exhibit inferior cyclic performance for only 300 and 200 h, respectively. After the current rate is increased to 10 mA·cm^{-2}, the symmetrical batteries using Bi@NPCN-modified separator also exhibit the superior long-term cyclic stability for over 800 h, while the symmetrical batteries using NPCN-modified separator and pristine GF membrane fail after merely 190 and 130 h, respectively (Fig. 3(b)). In addition, the resistance characteristics of the symmetrical batteries using various separators after electrochemical tests were also examined, revealing the lowest charge transfer resistance of those using Bi@NPCN-modified separator (Fig. S6 in the ESM). The rate performance of these symmetrical batteries was also measured from 1 to 20 mA·cm^{-2} (Fig. 3(c)). Excitingly, the symmetrical batteries using Bi@NPCN-modified separator deliver stable voltage polarization even under 20 mA·cm^{-2}. However, the symmetrical batteries using NPCN-modified separator and pristine GF membrane show higher voltage polarizations under the same current rates. These results demonstrate that Bi@NPCN can realize highly stable and superior reversible Zn deposition behavior [41, 42].

The corrosion resistance of these symmetrical batteries was further investigated by measuring the linear polarization curves. As displayed in Fig. S7 in the ESM, the Zn/Bi@NPCN-based symmetrical batteries exhibit a corrosion current density of 3.98 mA·cm^{-2}, much lower than those of Zn/NPCN-based (5.64 mA·cm^{-2}) and bare Zn-based (5.83 mA·cm^{-2}) symmetrical batteries. This demonstrates that Bi@NPCN can better suppress the occurrence of Zn corrosion [43, 44]. Moreover, the Zn deposition behaviors on Zn/Bi@NPCN, Zn/NPCN, and bare Zn surface were examined by testing the cyclic voltammetry (CV) curves of Zn/Bi@NPCN//Ti, Zn/NPCN//Ti, and bare Zn//Ti cells, and the potential between A and B indicates the trend for uniform Zn deposition. As clearly shown in Fig. S8 in the ESM, the potential between A and B for Zn/Bi@NPCN//Ti cell is only 28 mV, much lower than those of Zn/NPCN//Ti (51 mV) and bare Zn//Ti cells (62 mV), demonstrating that Bi@NPCN can efficiently guide uniform Zn deposition [45, 46]. In addition, chronoamperometry technique was further conducted to verify Zn deposition behavior, and Fig. S9 in the ESM displays the current–time curves of these symmetrical batteries. After the two-dimensional (2D) Zn deposition for ~ 100 s, Zn/Bi@NPCN anode started the three-dimensional (3D) Zn deposition, implying a uniform Zn deposition on Bi@NPCN surface. However, Zn/NPCN anode exhibits a 2D Zn deposition for more than 200 s, and bare Zn anode shows a continuous current decrease. These longer time for 2D Zn deposition may induce the formation and growth of Zn dendrites [47, 48].

Asymmetrical batteries were then assembled to further assess the

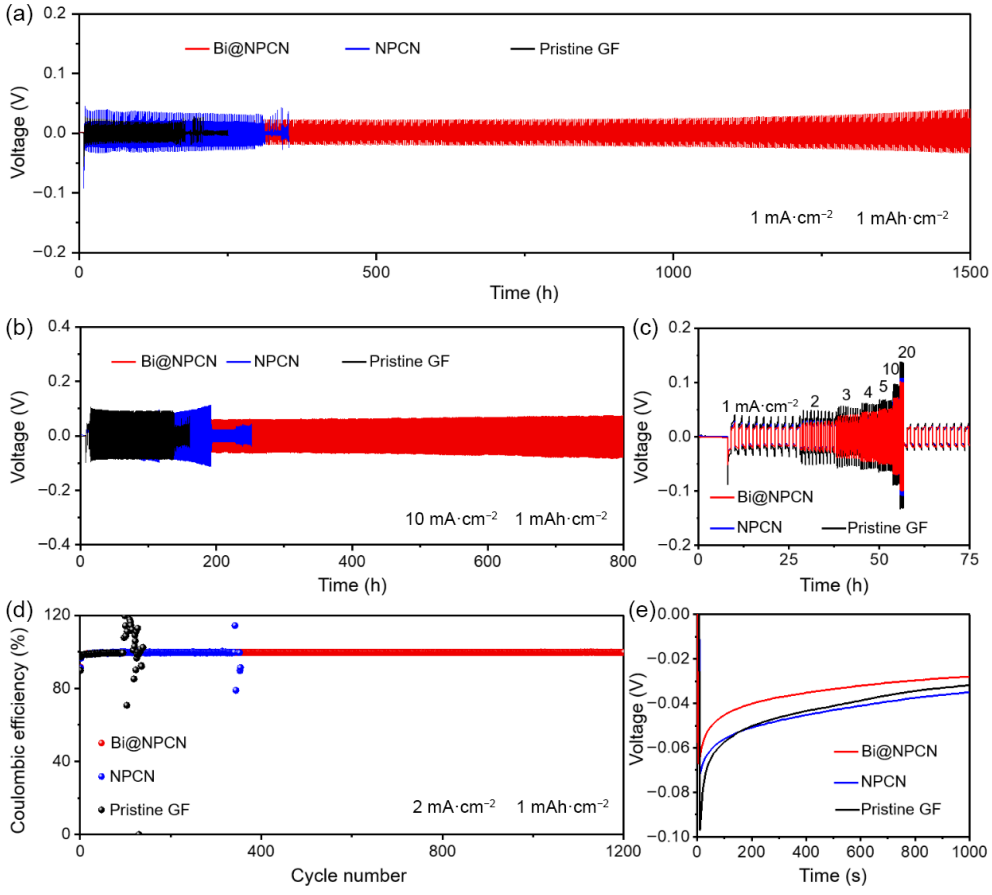

Figure 3 Electrochemical performance of Zn metal anodes using various separators. Cyclic performance of symmetrical batteries using various separators at (a) 1 and (b) 10 mA·cm^{-2}. (c) Rate performance of symmetrical batteries using various separators. (d) Coulombic efficiencies and (e) Zn nucleation potential of asymmetrical batteries using various separators at 2 mA·cm^{-2}.

Zn deposition behaviors on Bi@NPCN. Moreover, asymmetrical batteries using NPCN-modified separator and pristine GF membrane were tested. As presented in Fig. 3(d), the asymmetrical batteries using Bi@NPCN-modified separator exhibit superior Coulombic efficiency approaching 100% and an ultra-stable long-term cycle for over 1200 cycles under 2 mA·cm^{-2} and 1 mAh·cm^{-2}. As a sharp contrast, the asymmetric batteries using NPCN-modified separator and pristine GF membrane display the cyclic performance for only 370 and 120 cycles, respectively, and then they suffer from apparent efficiency fluctuations. Moreover, Zn nucleation potential is an important indicator for estimating Zn deposition behavior. Obviously, the Zn nucleation potential on Bi@NPCN is about 35 mV, lower than those on NPCN (43 mV) and bare Zn foil (71 mV) (Fig. 3(e)), indicating that Bi@NPCN can better facilitate Zn deposition [49]. Notably, the decreased Zn nucleation on NPCN as compared to bare Zn foil is ascribed to the decreased local current density originating from its high surface area, while the further reduced Zn nucleation potential on Bi@NPCN can be attributed to the existence of abundant nuclei stemming from Bi nanoparticles [50, 51]. Therefore, Bi@NPCN can better guide homogeneous Zn deposition and enable the stable cyclic performance of batteries.

In situ optical microscopy was then conducted to visually verify the functions of Bi@NPCN and NPCN during Zn plating. The Bi@NPCN and NPCN were coated on Zn foil with a thickness of ~ 10 μm, and the Zn deposition test was performed on a homemade cell under a high current density of 10 mA·cm^{-2}. As presented in Fig. 4(a), bare Zn foil suffers from an apparent dendrite formation only 4 min after the test started, and after 15 min, dense and long Zn dendrites were achieved on Zn surface. For Zn foil coated with NPCN layer (Fig. 4(b)), Zn initially deposited on the NPCN layer, and a Zn layer was formed after only 6 min. After 15 min, a dense Zn layer with dendrites formed on surface was gained. As a sharp contrast, for Zn foil coated with a Bi@NPCN layer, a smooth and dendrite-free surface was achieved even after 15 min (Fig. 4(c)), indicating that Bi@NPCN layer can efficiently suppress dendrite formation and growth. These observed Zn deposition behaviors can be attributed to the surface difference between Zn foils. As illustrated in Fig. 4(d), the uneven galvanization is distributed on bare Zn foil owing to the side reactions including corrosion, passivation, and hydrogen evolution reaction [52], which inevitably induce the Zn dendrite formation and growth on Zn foil surface. For Zn foil coated with NPCN layer (Fig. 4(e)), Zn deposition occurs on the surface of NPCN layer because of the induced homogeneous electric fields by NPCN layer. However, Zn dendrites generated on Zn layer during continuous

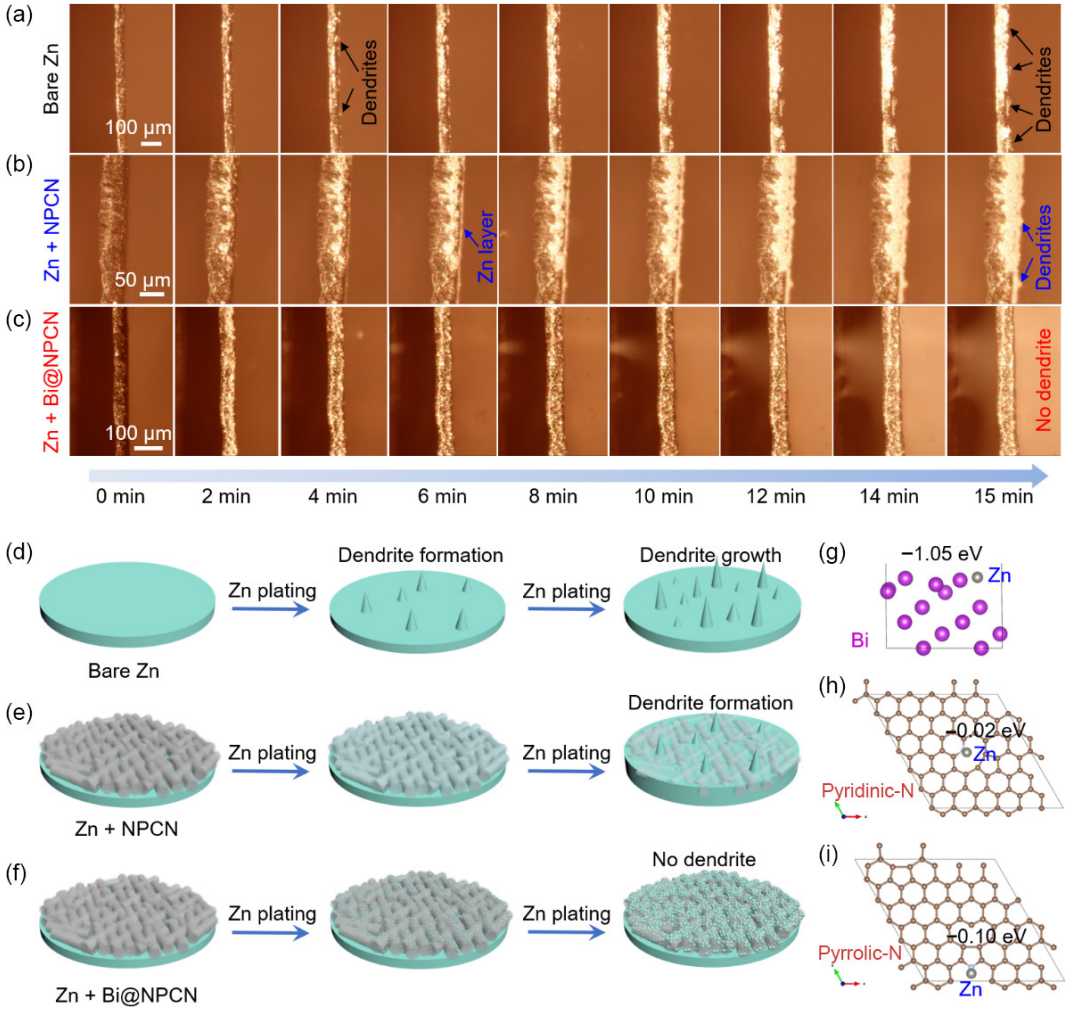

Figure 4 The Zn deposition behaviors in the case of different coating layers during plating. *In situ* optical microscopy of (a) bare Zn, (b) Zn with NPCN layer, and (c) Zn with Bi@NPCN layer at 10 mA·cm^{-2}. Schematic illustrations of the Zn deposition behaviors on (d) bare Zn, (e) Zn with NPCN layer, and (f) Zn with Bi@NPCN layer during plating. The adsorption models of Zn atoms on (g) Bi, (h) pyridinic-N, and (i) pyrrolic-N structures.

plating, while for Zn foil coated with Bi@NPCN layer (Fig. 4(f)), Bi nanoparticles strongly adsorbed Zn^{2+} due to the high zincophilic property originating from the higher binding energy between Bi structure and Zn atom (Fig. 4(g)), compared to those of N groups with Zn atoms (Figs. 4(h) and 4(i) and Fig. S10 in the ESM), and Zn deposition may initially occur around Bi nanoparticles instead of Bi@NPCN surface. Considering the multicore–shell structure of Bi@NPCN and sufficient space between Bi nanoparticles and carbon, maybe no Zn was deposited on Bi@NPCN surface.

To further evaluate the possibility for practical utilizations of Bi@NPCN, Zn-ion batteries using Zn anode, $NH_4V_4O_{10}$ cathode [53] (Figs. S11 and S12 in the ESM), and modified GF membrane were then assembled and tested. Figure 5(a) shows the typical CV curves of Zn-ion batteries within 0.3–1.4 V at 0.1 mV·s^{-1}. The Zn-ion batteries using Bi@NPCN-modified separator and pristine GF membrane display the typical CV shapes of $NH_4V_4O_{10}$ cathode with comparable peak current densities [54, 55]. The rate performance of Zn-ion batteries using different separators were measured with the current densities ranging from 0.5 to 10 A·g^{-1}. As presented in Fig. 5(b), Zn-ion batteries using Bi@NPCN-modified separator exhibit a slightly higher rate capability compared to Zn-ion batteries using pristine GF membrane, and the specific capacities at 0.5, 1.0, 2.0, 3.0, 5.0, and 10 A·g^{-1} are 304, 282, 265, 240, 208, and 161 mAh·g^{-1}, respectively. When the current rate was reset to 0.5 A·g^{-1}, the specific capacity recovered to 298 mAh·g^{-1}, while for Zn-ion batteries using pristine GF membrane, the specific capacity at 10 A·g^{-1} is 152 mAh·g^{-1}.

The long-term cyclic performance of Zn-ion batteries under high rates can better reflect the practical availability of Zn anode. As shown in Fig. 5(c), the Zn-ion batteries using Bi@NPCN-modified separator deliver a stable cyclic performance for over 500 cycles at 2.0 A·g^{-1}. After 500 cycles, the specific capacity retains at 228 mAh·g^{-1}, corresponding to a high capacity retention of 76.3%. As a contrast, the Zn-ion batteries using pristine GF membrane display a specific capacity of only 206 mAh·g^{-1} at the 500th cycle. After the current rate is increased to 5.0 A·g^{-1}, Zn-ion batteries using Bi@NPCN-modified separator exhibit an ultra-stable cyclic performance for over 3000 cycles (Fig. 5(d)). After the initial activation process, the specific capacity at 5.0 A·g^{-1} reaches 198 mAh·g^{-1} and then keeps almost stable after 700 cycles. In the residual cycles, the specific capacity decreases gradually, and eventually it retains at 132 mAh·g^{-1} after 3000 cycles, indicating a high capacity retention of 66.7%. Moreover, the Coulombic efficiency at the 3000th cycle approaches 100%, suggesting the high reversibility of Zn-ion batteries. For comparison, Zn-ion batteries using pristine GF membrane show lower specific capacity values with battery failure for only ~ 1200 cycles. The cyclic performance of Zn-ion batteries under high areal loading of $NH_4V_4O_{10}$ was also tested. As shown in Fig. 5(e), after the activation process, the Zn-ion batteries under 10 mg·cm^{-2} $NH_4V_4O_{10}$ exhibit an initial specific capacity of 173 mAh·g^{-1} at 1.0 A·g^{-1}. Then, the specific capacity increases gradually during the first 400 cycles, and finally, the specific capacity reaches 191 mAh·g^{-1} at the 400th cycle. The increment of specific capacity can be attributed to the activation process of $NH_4V_4O_{10}$ cathode, which enables the thorough electrolyte penetration and complete contact between electrolyte

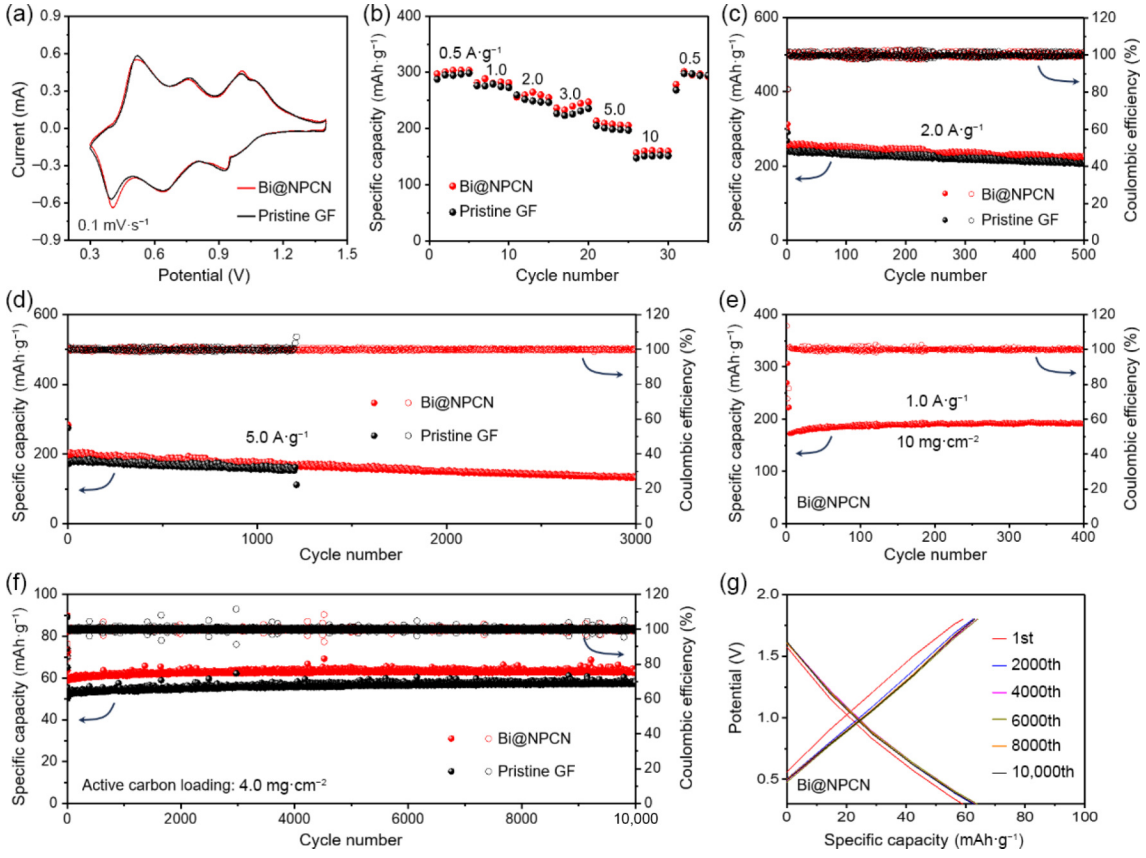

Figure 5 Electrochemical performance of Zn-ion batteries using $NH_4V_4O_{10}$ and active carbon as cathode materials. (a) CV curves, (b) rate capability, and cyclic performances at (c) 2.0 and (d) 5.0 A·g^{-1} for Zn-ion batteries using $NH_4V_4O_{10}$ cathode. (e) Cyclic performance of Zn-ion batteries under 10 mg·cm^{-2} $NH_4V_4O_{10}$ at 1.0 A·g^{-1}. (f) Cyclic performance of Zn-ion batteries using active carbon cathode at 5.0 A·g^{-1} and (g) the galvanostatic discharge/charge profiles at different cycles.

and $NH_4V_4O_{10}$. As a sharp contrast, Zn-ion batteries using pristine GF membrane presented lower specific capacities and failed after only 70 cycles (Fig. S13 in the ESM).

The Zn-ion batteries using active carbon as cathode were also assessed. Figure 5(f) shows the cyclic performance of Zn-ion batteries under 4.0 mg·cm^{-2} active carbon at 5.0 A·g^{-1}. Apparently, Zn-ion batteries using Bi@NPCN-modified separator exhibit comparable long-term cyclic performance with higher specific capacity values for 10,000 cycles, compared to Zn-ion batteries using pristine GF membrane. Initially, Zn-ion batteries using Bi@NPCN-modified separator deliver a high specific capacity of 61 mAh·g^{-1}, and then the specific capacity keeps almost stable and maintains at 63 mAh·g^{-1} at the 10,000th cycle. For comparison, Zn-ion batteries using pristine GF membrane show a specific capacity of 58 mAh·g^{-1} after running 10,000 cycles. Notably, the Coulombic efficiency of Zn-ion batteries using Bi@NPCN-modified separator at the 10,000th cycle is ~ 100%, implying the high reversibility of Zn metal anode. Figure 5(g) shows the galvanostatic discharge/charge profiles of Zn-ion batteries using Bi@NPCN-modified separator at different cycles, disclosing the typical profile shape of Zn-ion batteries using active carbon [27]. Moreover, these profiles show the similar shape characteristics, further suggesting the high reversibility of Zn-ion batteries. Therefore, it is concluded that Bi@NPCN ameliorated the electrochemical performance of Zn-ion batteries, which is attributed to the significantly improved Zn utilization efficiency.

3 Conclusions

In summary, a multicore–shell Bi@NPCN was designed and constructed to efficiently regulate Zn deposition behaviors. Benefitting from the high zincophilic property of Bi nanoparticles and porous feature of NPCN, Bi@NPCN enabled a rapid dendrite-free Zn deposition, as confirmed by theoretical simulations and *in situ* optical microscopy test. Electrochemical measurements reveal an ultra-stable Zn deposition behavior for over 1500 h and an exceptional Coulombic efficiency of ~ 100% for 1200 cycles, with a low hysteresis voltage of only 35 mV. Consequently, the Zn-ion batteries coupled with $NH_4V_4O_{10}$ cathode exhibit an impressive cyclic performance for 3000 cycles. Moreover, a highly stable cyclic performance for over 10,000 cycles was achieved when using active carbon as cathode material. This study demonstrates that the multicore–shell structure with abundant zincophilic seeding sites can realize high-performance and dendrite-free Zn metal anodes.

Electronic Supplementary Material: Supplementary material (synthesis methods, electrochemical testing details, theoretical studies, and Figs. S1–S13) is available in the online version of this article at https://doi.org/10.26599/NR.2025.94907372.

Data availability

All data needed to support the conclusions in the paper are presented in the manuscript and the ESM. Additional data related to this paper may be requested from the corresponding author upon request.

Acknowledgements

The authors appreciate the financial support from the National Natural Science Foundation of China (No. 52201222), the Natural Science Research Project of Anhui Province Education Department (No. 2022AH030046), and the Project of High-End Talent Introduction and Cultivation in Anhui Province. This work is supported by High-performance Computing Public Platform (Shenzhen Campus) of Sun Yat-sen University.

Declaration of competing interest

All the contributing authors report no conflict of interests in this work.

Author contribution statement

Y. S. Z. and Y. L. conducted the experiments and tested the electrochemical performance. X. Z. helped to measure the electrochemical performance. J. X. and B. P. analyzed the electrochemical results. G. Y. Z. tested the *in situ* measurements and revised the manuscript. J. P. L. conducted the theoretical simulations and revised the manuscript. L. B. M. provided funding support, analyzed the results, wrote and revised the manuscript.

Use of AI statement

None.

References

[1] Etacheri, V.; Marom, R.; Elazari, R.; Salitra, G.; Aurbach, D. Challenges in the development of advanced Li-ion batteries: A review. *Energy Environ. Sci.* **2011**, *4*, 3243–3262.

[2] Nitta, N.; Wu, F. X.; Lee, J. T.; Yushin, G. Li-ion battery materials: Present and future. *Mater. Today* **2015**, *18*, 252–264.

[3] Ma, L. B.; Wu, Q. Z.; He, M.; Wu, J. X.; Peng, B.; Xu, J.; Liu, J. P.; Jin, Z. Binary metal alloy electrocatalyst synergistically accelerates the bidirectional polysulfide conversions in lithium-sulfur batteries. *Nano Lett.* **2025**, *25*, 1939–1947.

[4] Palomares, V.; Serras, P.; Villaluenga, I.; Hueso, K. B.; Carretero-Gonzalez, J.; Rojo, T. Na-ion batteries, recent advances and present challenges to become low cost energy storage systems. *Energy Environ. Sci.* **2012**, *5*, 5884–5901.

[5] Fang, G. Z.; Zhou, J.; Pan, A. Q.; Liang, S. Q. Recent advances in aqueous zinc-ion batteries. *ACS Energy Lett.* **2018**, *3*, 2480–2501.

[6] Zhang, N.; Chen, X. Y.; Yu, M.; Niu, Z. Q.; Cheng, F. Y.; Chen, J. Materials chemistry for rechargeable zinc-ion batteries. *Chem. Soc. Rev.* **2020**, *49*, 4203–4219.

[7] Bai, Z. C.; Wang, G. L.; Liu, H. M.; Lou, Y. T.; Wang, N. N.; Liu, H. K.; Dou, S. X. Advancements in aqueous zinc-iodine batteries: A review. *Chem. Sci.* **2024**, *15*, 3071–3092.

[8] Chen, H.; Li, X.; Fang, K. Q.; Wang, H. Y.; Ning, J. Q.; Hu, Y. Aqueous zinc-iodine batteries: From electrochemistry to energy storage mechanism. *Adv. Energy Mater.* **2023**, *13*, 2302187.

[9] Tang, R. R.; Yang, Y.; Zhou, Y. T.; Yu, X. Y. Rational design of heterostructured Ru cluster-based catalyst for pH universal hydrogen evolution reaction and high-performance Zn-H_2O battery. *Adv. Funct. Mater.* **2024**, *34*, 2301925.

[10] Li, H. B.; Cao, M. G.; Fu, Z. L.; Ma, Q. W.; Zhang, L. H.; Wang, R.; Liang, F.; Zhou, T. F.; Zhang, C. F. A covalent organic framework as a dual-active-center cathode for a high-performance aqueous zinc-ion battery. *Chem. Sci.* **2024**, *15*, 4341–4348.

[11] Zhang, M. M.; Wei, H. Y.; Zhou, Y. T.; Wen, W. D.; Zhang, L.; Yu, X. Y. A multi-functional protective material with atomically dispersed zincophilic sites enabling long-life zinc anodes. *Chem. Sci.* **2024**, *15*, 18187–18195.

[12] Li, L. Y.; Zheng, Y. S.; Xu, J.; Peng, B.; Zhu, G. Y.; Wu, J. X.; Ma, L.

B.; Jin, Z. Structural and interfacial engineering strategies for constructing dendrite-free zinc metal anodes. *ACS Energy Lett.* **2024**, *9*, 3269–3289.

[13] Cheng, Z. H.; Wang, K.; Fu, J. M.; Mo, F. N.; Lu, P.; Gao, J. T.; Ho, D.; Li, B.; Hu, H. B. Texture exposure of unconventional $(101)_{Zn}$ facet: Enabling dendrite-free Zn deposition on metallic zinc anode. *Adv. Energy Mater.* **2024**, *14*, 2304003.

[14] Shin, J.; Lee, J.; Park, Y.; Choi, J. W. Aqueous zinc ion batteries: Focus on zinc metal anodes. *Chem. Sci.* **2020**, *11*, 2028–2044.

[15] Tang, B. Y.; Shan, L. T.; Liang, S. Q.; Zhou, J. Issues and opportunities facing aqueous zinc-ion batteries. *Energy Environ. Sci.* **2019**, *12*, 3288–3304.

[16] Yi, Z. H.; Chen, G. Y.; Hou, F.; Wang, L. Q.; Liang, J. Strategies for the stabilization of Zn metal anodes for Zn-ion batteries. *Adv. Energy Mater.* **2021**, *11*, 2003065.

[17] Jia, H.; Wang, Z. Q.; Tawiah, B.; Wang, Y. D.; Chan, C. Y.; Fei, B.; Pan, F. Recent advances in zinc anodes for high-performance aqueous Zn-ion batteries. *Nano Energy* **2020**, *70*, 104523.

[18] Ma, L. B.; Cui, J.; Yao, S. S.; Liu, X. M.; Luo, Y. S.; Shen, X. P.; Kim, J. K. Dendrite-free lithium metal and sodium metal batteries. *Energy Storage Mater.* **2020**, *27*, 522–554.

[19] Cheng, X. B.; Zhang, R.; Zhao, C. Z.; Zhang, Q. Toward safe lithium metal anode in rechargeable batteries: A review. *Chem. Rev.* **2017**, *117*, 10403–10473.

[20] Guo, N.; Huo, W. J.; Dong, X. Y.; Sun, Z. F.; Lu, Y. T.; Wu, X. W.; Dai, L.; Wang, L.; Lin, H. C.; Liu, H. D. et al. A review on 3D zinc anodes for zinc ion batteries. *Small Methods* **2022**, *6*, 2200597.

[21] Nie, C. H.; Wang, G. L.; Wang, D. D.; Wang, M. Y.; Gao, X. R.; Bai, Z. C.; Wang, N. N.; Yang, J.; Xing, Z.; Dou, S. X. Recent progress on Zn anodes for advanced aqueous zinc-ion batteries. *Adv. Energy Mater.* **2023**, *13*, 2300606.

[22] Mao, C. W.; Chang, Y. X.; Zhao, X. T.; Dong, X. Y.; Geng, Y. F.; Zhang, N.; Dai, L.; Wu, X. W.; Wang, L.; He, Z. X. Functional carbon materials for high-performance Zn metal anodes. *J. Energy Chem.* **2022**, *75*, 135–153.

[23] Yang, S. N.; Du, H. X.; Li, Y. T.; Wu, X. S.; Xiao, B. S.; He, Z. X.; Zhang, Q. B.; Wu, X. W. Advances in the structure design of substrate materials for zinc anode of aqueous zinc ion batteries. *Green Energy Environ.* **2023**, *8*, 1531–1552.

[24] Nie, W.; Cheng, H. W.; Sun, Q. C.; Liang, S. Q.; Lu, X. G.; Lu, B. A.; Zhou, J. Design strategies toward high-performance Zn metal anode. *Small Methods* **2024**, *8*, 2201572.

[25] Gong, Y. X.; Wang, B.; Ren, H. Z.; Li, D. Y.; Wang, D. L.; Liu, H. K.; Dou, S. X. Recent advances in structural optimization and surface modification on current collectors for high-performance zinc anode: Principles, strategies, and challenges. *Nano-Micro Lett.* **2023**, *15*, 208.

[26] Cui, Y. W.; Ju, Z. Y.; Yu, R. F.; Du, H. P.; Zhang, B. W.; Wang, Y. Q.; Yu, G. H. Challenges, strategies, and perspectives of anode protection in aqueous zinc-ion batteries. *ACS Mater. Lett.* **2024**, *6*, 611–626.

[27] Zhu, G. Y.; Zhang, H. C.; Lu, J. Q.; Hou, Y. N.; Liu, P.; Dong, S. Y.; Pang, H.; Zhang, Y. Z. 3D printing of MXene-enhanced ferroelectric polymer for ultrastable zinc anodes. *Adv. Funct. Mater.* **2024**, *34*, 2305550.

[28] Liu, F. Y.; Zhang, Y. Q.; Liu, H.; Zhang, S. X.; Yang, J. Y.; Li, Z.; Huang, Y. H.; Ren, Y. Advances of nanomaterials for high-efficiency Zn metal anodes in aqueous zinc-ion batteries. *ACS Nano* **2024**, *18*, 16063–16090.

[29] Li, H. P.; Guo, C.; Zhang, T. S.; Xue, P.; Zhao, R. Z.; Zhou, W. H.; Li, W.; Elzatahry, A.; Zhao, D. Y.; Chao, D. L. Hierarchical confinement effect with zincophilic and spatial traps stabilized Zn-based aqueous battery. *Nano Lett.* **2022**, *22*, 4223–4231.

[30] Chen, T.; Wang, Y. N.; Yang, Y.; Huang, F.; Zhu, M. K.; Ang, B. T. W.; Xue, J. M. Heterometallic seed-mediated zinc deposition on inkjet printed silver nanoparticles toward foldable and heat-resistant zinc batteries. *Adv. Funct. Mater.* **2021**, *31*, 2101607.

[31] Kim, H. J.; Kim, S.; Kim, S.; Kim, S.; Heo, K.; Lim, J. H.; Yashio, H.; Shin, H. J.; Jung, H. G.; Lee, Y. M. et al. Gold-nanolayer-derived zincophilicity suppressing metallic zinc dendrites and its efficacy in improving electrochemical stability of aqueous zinc-ion batteries. *Adv. Mater.* **2024**, *36*, 2308592.

[32] Yang, S. N.; Li, Y. T.; Du, H. X.; Liu, Y. Q.; Xiang, Y. H.; Xiong, L. Z.; Wu, X. M.; Wu, X. W. Copper nanoparticle-modified carbon nanofiber for seeded zinc deposition enables stable Zn metal anode. *ACS Sustain. Chem. Eng.* **2022**, *10*, 12630–12641.

[33] Yu, H.; Zeng, Y. X.; Li, N. W.; Luan, D. Y.; Yu, L.; Lou, X. W. Confining Sn nanoparticles in interconnected N-doped hollow carbon spheres as hierarchical zincophilic fibers for dendrite-free Zn metal anodes. *Sci. Adv.* **2022**, *8*, eabm5766.

[34] Zhang, X. R.; Qu, C. Z.; Zhang, X. H.; Peng, X.; Qiu, Y. Q.; Su, Y. X.; Zeng, J. R.; Liu, Z.; Liu, X. R.; Qi, W. H. et al. Atomic Sn encapsulation with visualizing mitigated active zinc loss toward anode-lean zinc metal battery. *Adv. Energy Mater.* **2024**, *14*, 2401139.

[35] Wang, J. H.; Chen, L. F.; Dong, W. X.; Zhang, K. L.; Qu, Y. F.; Qian, J. W.; Yu, S. H. Three-dimensional zinc-seeded carbon nanofiber architectures as lightweight and flexible hosts for a highly reversible zinc metal anode. *ACS Nano* **2023**, *17*, 19087–19097.

[36] Ma, L. B.; Zhu, G. Y.; Wang, Z. W.; Zhu, A. C.; Wu, K. L.; Peng, B.; Xu, J.; Wang, D. H.; Jin, Z. Long-lasting zinc-iodine batteries with ultrahigh areal capacity and boosted rate capability enabled by nickel single-atom electrocatalysts. *Nano Lett.* **2023**, *23*, 5272–5280.

[37] Li, Z. L.; Deng, L. B.; Kinloch, I. A.; Young, R. J. Raman spectroscopy of carbon materials and their composites: Graphene, nanotubes and fibres. *Prog. Mater. Sci.* **2023**, *135*, 101089.

[38] Lv, Q.; Si, W. Y.; He, J. J.; Sun, L.; Zhang, C. F.; Wang, N.; Yang, Z.; Li, X. D.; Wang, X.; Deng, W. Q. et al. Selectively nitrogen-doped carbon materials as superior metal-free catalysts for oxygen reduction. *Nat. Commun.* **2018**, *9*, 3376.

[39] Xiong, P. X.; Bai, P. X.; Li, A.; Li, B. F.; Cheng, M. R.; Chen, Y. P.; Huang, S. P.; Jiang, Q.; Bu, X. H.; Xu, Y. H. Bismuth nanoparticle@carbon composite anodes for ultralong cycle life and high-rate sodium-ion batteries. *Adv. Mater.* **2019**, *31*, 1904771.

[40] Chen, Z. L.; Wu, X. Y.; Sun, Z. F.; Pan, J. H.; Han, J. J.; Wang, Y. S.; Liu, H. D.; Shen, Y. B.; Li, J.; Peng, D. L. et al. Enhanced fast-charging and longevity in sodium-ion batteries through nitrogen-doped carbon frameworks encasing flower-like bismuth microspheres. *Adv. Energy Mater.* **2024**, *14*, 2400132.

[41] Zhang, X. T.; Li, J. X.; Liu, Y. F.; Lu, B. A.; Liang, S. Q.; Zhou, J. Single [0001]-oriented zinc metal anode enables sustainable zinc batteries. *Nat. Commun.* **2024**, *15*, 2735.

[42] Wang, F.; Borodin, O.; Gao, T.; Fan, X. L.; Sun, W.; Han, F. D.; Faraone, A.; Dura, J. A.; Xu, K.; Wang, C. S. Highly reversible zinc metal anode for aqueous batteries. *Nat. Mater.* **2018**, *17*, 543–549.

[43] Na, Z. L.; Qi, H. K.; Li, S. H.; Wu, Y. B.; Wang, Q. S.; Huang, G. Stable zinc metal anode by nanosecond pulsed laser enabled gradient design. *ACS Energy Lett.* **2023**, *8*, 3297–3306.

[44] Chen, J. Y.; Qiao, X.; Han, X. R.; Zhang, J. H.; Wu, H. B.; He, Q.; Chen, Z. B.; Shi, L.; Wang, Y. Z.; Xie, Y. N. et al. Releasing plating-induced stress for highly reversible aqueous Zn metal anodes. *Nano Energy* **2022**, *103*, 107814.

[45] Zhang, J. Z.; Zhao, Q. Y.; Wei, X.; Li, A. J.; Xu, H.; Chen, G.; Zheng, Y. S.; Xu, Y. T.; Wang, X. F. Crystallographic customization of zinc anode for high performance aqueous metal batteries. *Nano Lett.* **2025**, *25*, 648–654.

[46] Zhang, L. Q.; Huang, J. J.; Guo, H. L.; Ge, L. F.; Tian, Z. H.; Zhang, M. J.; Wang, J. T.; He, G. J.; Liu, T. X.; Hofkens, J. et al. Tuning ion transport at the anode–electrolyte interface via a sulfonate-rich ion-exchange layer for durable zinc-iodine batteries. *Adv. Energy Mater.* **2023**, *13*, 2203790.

[47] Zhang, W.; Dai, Y. H.; Chen, R. W.; Xu, Z. M.; Li, J. W.; Zong, W.; Li, H. X.; Li, Z.; Zhang, Z. Y.; Zhu, J. X. et al. Highly reversible zinc metal anode in a dilute aqueous electrolyte enabled by a pH buffer additive. *Angew. Chem., Int. Ed.* **2023**, *62*, e202212695.

[48] Zou, P. C.; Zhang, R.; Yao, L. B.; Qin, J. Y.; Kisslinger, K.; Zhuang, H. L.; Xin, H. L. Ultrahigh-rate and long-life zinc-metal anodes enabled by self-accelerated cation migration. *Adv. Energy Mater.* **2021**, *11*, 2100982.

[49] Du, Y. X.; Feng, Y.; Li, R. T.; Peng, Z.; Yao, X. Y.; Duan, S. Y.; Liu, S. D.; Jun, S. C.; Zhu, J.; Dai, L. et al. Zinc–bismuth binary alloy enabling high-performance aqueous zinc ion batteries. *Small* **2024**, *20*, 2307848.

[50] Yang, Z. F.; Zhang, Q.; Li, W. B.; Xie, C. L.; Wu, T. Q.; Hu, C.; Tang, Y. G.; Wang, H. Y. A semi-solid zinc powder-based slurry anode for advanced aqueous zinc-ion batteries. *Angew. Chem., Int. Ed.* **2023**, *62*, e202215306.

[51] Chen, H. L.; Zhang, W. Y.; Yi, S.; Su, Z.; Zhao, Z. Q.; Zhang, Y. Y.; Niu, B.; Long, D. H. Zinc iso-plating/stripping: Toward a practical Zn powder anode with ultra-long life over 5600 h. *Energy Environ. Sci.* **2024**, *17*, 3146–3156.

[52] Fan, C. C.; Meng, W. J.; Ye, J. Y. Towards advanced zinc anodes by interfacial modification strategies for efficient aqueous zinc metal batteries. *J. Energy Chem.* **2024**, *93*, 79–110.

[53] Xu, D. M.; Wang, Z.; Liu, C. J.; Li, H. Y.; Ouyang, F.; Chen, B. Q.; Li, W. H.; Ren, X. T.; Bai, L. S.; Chang, Z. et al. Water catchers within sub-nano channels promote step-by-step zinc-ion dehydration enable highly efficient aqueous zinc-metal batteries. *Adv. Mater.* **2024**, *36*, 2403765.

[54] Chen, S.; Ji, D. L.; Chen, Q. W.; Ma, J. Z.; Hou, S. Q.; Zhang, J. T. Coordination modulation of hydrated zinc ions to enhance redox reversibility of zinc batteries. *Nat. Commun.* **2023**, *14*, 3526.

[55] Xu, J.; Dai, Q. Y.; Yang, Y. T.; Zheng, Z. Y.; Yu, F. T.; Cao, Y. J.; Jiang, Z. P.; Peng, B.; Ma, L. B. Wide-temperature zinc-iodine batteries enabling by a Zn-ion conducting covalent organic framework buffer layer. *Chem. Eng. J.* **2024**, *502*, 157984.